The performance of implicit ocean models on B- and C-grids

Fred W. Wubs [a,*], Arie C. de Niet [a], Henk A. Dijkstra [b,c]

[a] *Research Institute for Mathematics and Computing Science, University of Groningen, Blauwborgje 3,*
9747 AC Groningen, the Netherlands
[b] *Department of Atmospheric Science, Colorado State University, Fort Collins, CO 80523, USA*
[c] *Institute for Marine and Atmospheric Research Utrecht, Department of Physics and Astronomy, Utrecht University,*
Utrecht, the Netherlands

Abstract

Fully-implicit primitive equation ocean models are useful to study the sensitivity of steady ocean flows to parameters, to determine bifurcations of these flows associated with instabilities and to use relatively large time steps in transient flow computations. This paper addresses a problem related to the origin of wiggles occurring in fully-implicit C-grid models. The situation considered is the computation of three-dimensional thermally-driven steady flows in a midlatitude spherical sector. We determine the reason why in a coarse resolution C-grid implicit model, the values of the lateral friction coefficients are restricted to far higher values than for the same B-grid model. The analysis also reveals why the B-grid discretization is superior for the computation of this type of flows.
© 2005 Elsevier Inc. All rights reserved.

1. Introduction

Over the last decades many different large-scale ocean models have been developed, each with the aim to simulate the basin scale and/or global ocean circulation. They can be distinguished by the representation of the vertical structure of the flow, e.g. level models versus layer models, the type of horizontal grid, such as a B-grid or a C-grid, and the parameterizations of friction, diffusion, and convection. There are

---

low-resolution versions of these models, used for climate type studies, and high-resolution versions, used for detailed studies of the ocean currents [12].

Most of these models use an explicit time discretization, for example a leap-frog scheme or an Adams–Bashforth scheme, each having their typical constraint on the time step because of numerical stability. When the horizontal resolution is doubled in both directions in these models, the time step usually has to be decreased by a factor between 2 and 4. This factor, for example, depends on the type of representation of lateral friction in the models. When one is only interested in relatively short time intervals of simulation, this may not be a problem. To study the sensitivity of equilibrium large-scale ocean flows to forcing conditions or mixing representations, the computations may become extremely costly due to the very long equilibration time scale (in the order of thousand years) of the circulation.

Motivated by the problem of determining the sensitivity and stability of equilibrium flows, fully-implicit ocean models have been developed over the last decade [7,23]. One of the direct advantages of these methods is that relatively large time steps can be taken, since the time step is determined by accuracy instead of by numerical stability constraints. Another direct spin-off of the implicit formulation is the availability of the Jacobian matrix. This matrix can be used in a pseudo-arclength continuation method [14,17] to follow branches of steady states in parameter space. The Jacobian matrix is also needed to determine the linear stability problem of these steady states which can be determined by solving the corresponding generalized eigenvalue problem.

Since many readers may be unfamiliar with the continuation methodology as applied to ocean modeling, we sketch the relation of this approach to more traditional ocean modeling using a simple example. Consider the two-dimensional system of differential equations, given by

$$\frac{dx}{dt} = \lambda - x^2, \tag{1a}$$

$$\frac{dy}{dt} = x - y, \tag{1b}$$

where (x, y) are the state variables and λ is a parameter in the problem. When solved as an initial value problem, $x(t)$ and $y(t)$ are followed in time, for each $\lambda > 0$, until a steady state is reached. If for these values of λ, $x(t)$ is plotted in time, for the system (1) a plot as in Fig. 1(a) results. In each case, $x(t) \to \bar{x}$ for $t \to \infty$. To study sensitivity of the equilibria versus λ, only the end points $\bar{x}$ are of interest and typically one would show a plot as in Fig. 1(b).

With continuation methods one aims to directly compute the curve in Fig. 1(b) without going through the transient calculations as in Fig. 1(a). Instead of solving the time-dependent equations, these techniques directly tackle the steady equations, i.e. the model equations with the time-derivatives put to zero. For the example (1), these are

$$\lambda - \bar{x}^2 = 0, \tag{2a}$$

$$\bar{x} - \bar{y} = 0. \tag{2b}$$

Solving directly for the latter has one important additional advantage. For the steady states, we find $\bar{x} = \bar{y} = \sqrt{\lambda}$ and $\bar{x} = \bar{y} = -\sqrt{\lambda}$ for each value of $\lambda > 0$. However, looking at the evolution of small perturbations on these states, say

$$x = \bar{x} + \tilde{x}; \quad y = \bar{y} + \tilde{y}, \tag{3}$$

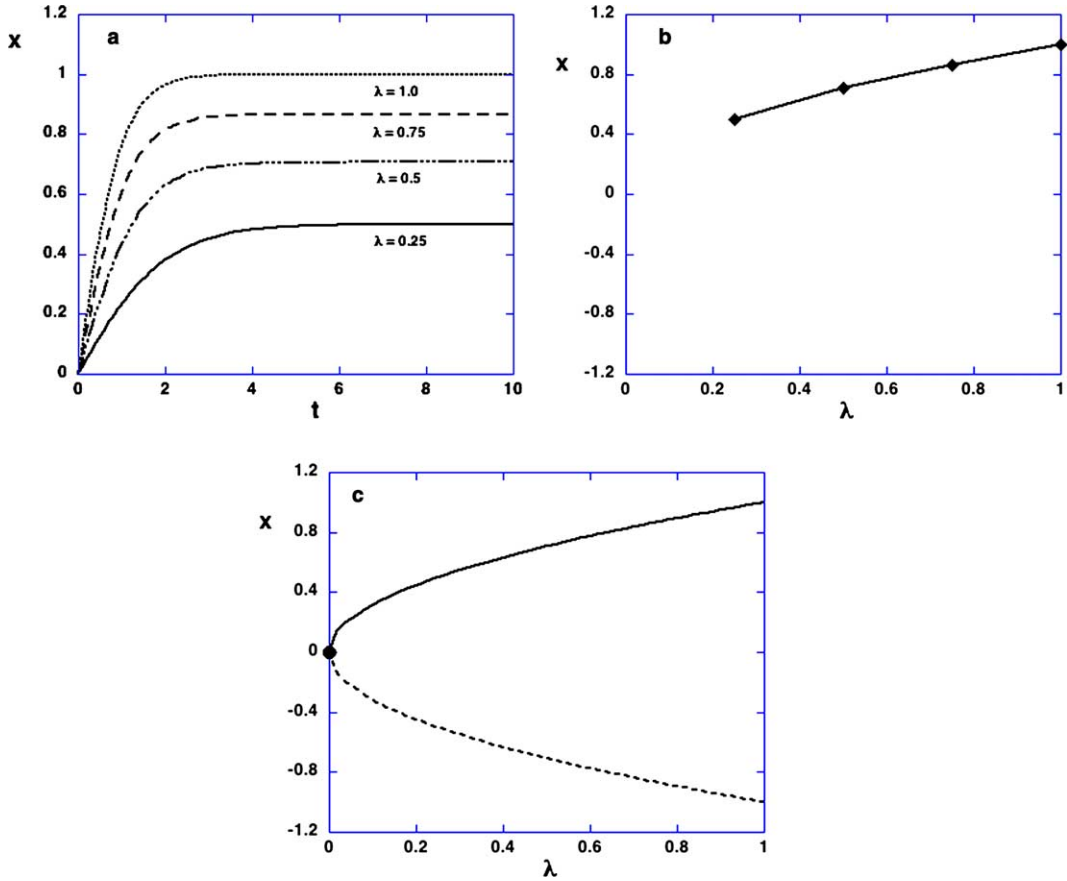the linearized equations from (1) are

Fig. 1. Solution of the system (1), with (a) transient solutions for several values of λ, (b) the steady state values of x versus λ and (c) the complete bifurcation diagram of (1).

$$\frac{\mathrm{d}\tilde{x}}{\mathrm{d}t} = (-2\bar{x})\tilde{x}, \tag{4a}$$

$$\frac{\mathrm{d}\tilde{y}}{\mathrm{d}t} = \tilde{x} - \tilde{y}. \tag{4b}$$

For the solution $\bar{x} = \bar{y} = \sqrt{\lambda}$, the perturbations will decay and hence the steady state is stable and it will be found by transient integration (as in Fig. 1(a)). The solution $\bar{x} = \bar{y} = -\sqrt{\lambda}$ is unstable since perturbations on it will grow and hence it will never be reached by the transient approach. However, by solving directly for the steady equations both solutions will be found, also the unstable one! In Fig. 1(c), the steady-state branches, as they are computed by continuation methods are plotted. Also the saddle-node bifurcation at $\bar{x} = \bar{y} = \lambda = 0$ can be explicitly computed with these techniques.

The application of continuation methods using fully-implicit ocean models [23] have helped clarify the role of multiple equilibria in rapid changes in the global ocean circulation induced by freshwater anomalies [6]. In addition, a start of a classification of oscillatory instabilities of basin wide and global ocean flows has been made [18]. One of these modes, with interdecadal period, has lead to an explanation of the physical mechanism of the Atlantic Multidecadal Oscillation [9]. Finally, implicit (Crank–Nicholson) time-stepping was used to determine thresholds for collapse of the thermohaline circulation in a fully-implicit global ocean model [8].

The implicit ocean models are, however, still far from state-of-the-art ocean models. For example, the representation of mixing processes of heat, salt and momentum is still limited to Laplacian formulations with constant (eddy) mixing coefficients. As shown in Weijer et al. [23], the magnitude of the coefficient of horizontal mixing of momentum, A_H, was quite restricted. Whereas in explicit low-resolution ocean general circulation models, $A_H = 2.5 \times 10^5 \, \mathrm{m}^2 \, \mathrm{s}^{-1}$ is used as a standard value on a $4° \times 4°$ horizontal resolution, strong wiggles are found in the fully-implicit model in Weijer et al. [23] for these values. Hence, the value of A_H used in Weijer et al. [23] was about a factor hundred larger than this standard value. By comparison with explicit model results, it was shown [19] that the thermohaline flow was not qualitatively affected by A_H. Nevertheless, the lack of an understanding of the underlying numerical problem has been quite unsatisfactory.

It is of interest to investigate whether this problem is due to the C-grid used or that it can be attributed to other sources. Also in explicit models, problems with the C-grid discretization have been noticed [13] and more practical fixes were suggested. The impact of different horizontal grids on transient ocean and atmospheric flows was already discussed in [2,3]. In Wajsowicz [21], the effect of the B- and C-grid discretization of the shallow-water equations on free wave propagation was addressed. It is shown, for example, that the dispersion relation of high-frequency waves is not well represented on the C-grid. In later studies, the properties of (discrete) Kelvin and planetary waves and their role in (numerical) ocean adjustment was determined [22,20,10,1].

In steady computations, the wiggles seem to be a lot worse than in transient computations as then wiggles extent over the whole domain instead of staying only locally along boundaries. In this paper, we focus on this numerical problem and study it for ocean flows in the single-hemispheric ocean basin configuration as in Dijkstra et al. [7]. The configuration is defined in Section 2 and typical computations of flows illustrating the numerical problems, are shown in Section 3. In Section 4, we present a detailed analysis of the problems of the implicit models on the C-grid and explain the restrictions on the magnitude of A_H. The analysis also reveals why these problems do not occur for implicit models on the B-grid.

2. Ocean flows in a single-hemispheric basin

The formulation of the implicit model and a discussion of the solution methods was presented in Dijkstra et al. [7]. It is, however, important that readers precisely know what equations are being solved without having to dig into previous papers. Hence the flow situation and the governing equations are briefly described below.

We consider ocean flows in a model domain on the sphere bounded by the longitudes $\phi_w = 84°\mathrm{W}$ and $\phi_e = 20°\mathrm{W}$ and by the latitudes $\theta_s = 10°\mathrm{N}$ and $\theta_n = 74°\mathrm{N}$; the ocean basin has a constant depth D. The flows in this domain are forced by a heat flux Q_H (in $\mathrm{W\,m}^{-2}$)

$$Q_H = -\mu(T - T_S), \tag{5}$$

where μ (in $\mathrm{W\,m}^{-2}\,\mathrm{K}^{-1}$) is a constant exchange coefficient. The heat flux Q_H is proportional to the temperature difference between the sea-surface temperature T and a prescribed atmospheric temperature T_S, chosen as

$$T_S(\phi, \theta) = T_0 + \frac{\Delta T}{2} \cos\left(\pi \frac{\theta - \theta_s}{\theta_n - \theta_s}\right), \tag{6}$$

where $T_0 = 15 \,°\mathrm{C}$ is a reference temperature and ΔT is the temperature difference between the southern and northern latitude of the domain. The forcing is distributed as a body forcing over the first (upper) layer of the ocean having a depth H_m.

Temperature differences in the ocean cause density differences according to

$$\rho = \rho_0(1 - \alpha_T(T - T_0)), \tag{7}$$

where α_T is the volumetric expansion coefficient and ρ_0 is a reference density. We neglect inertia in the momentum equations because of the small Rossby number, use the Boussinesq and hydrostatic approximations and represent horizontal and vertical mixing of momentum and heat by constant eddy coefficients. With r_0 and Ω being the radius and angular velocity of the Earth, the governing equations for the zonal, meridional and vertical velocity u, v and w and the dynamic pressure p (the hydrostatic part has been subtracted) become

$$-2\Omega v \sin\theta + \frac{1}{\rho_0 r_0 \cos\theta} \frac{\partial p}{\partial \phi} = A_V \frac{\partial^2 u}{\partial z^2} + A_H L_u(u,v), \tag{8a}$$

$$2\Omega u \sin\theta + \frac{1}{\rho_0 r_0} \frac{\partial p}{\partial \theta} = A_V \frac{\partial^2 v}{\partial z^2} + A_H L_v(u,v), \tag{8b}$$

$$\frac{\partial p}{\partial z} = \rho_0 g \alpha_T T, \tag{8c}$$

$$0 = \frac{\partial w}{\partial z} + \frac{1}{r_0 \cos\theta}\left(\frac{\partial u}{\partial \phi} + \frac{\partial(v\cos\theta)}{\partial \theta}\right), \tag{8d}$$

$$\frac{DT}{dt} - \nabla_H \cdot (K_H \nabla_H T) = \frac{\partial}{\partial z}\left(K_V \frac{\partial T}{\partial z}\right) + \frac{(T_S - T)}{\tau_T} \mathscr{H}\left(\frac{z}{H_m} + 1\right), \tag{8e}$$

where $\mathscr{H}$ is a continuous approximation of the Heaviside function, C_p the constant heat capacity and $\tau_T = \rho_0 C_p H_m / \mu$ is the surface adjustment time scale of heat. In these equations, A_H and A_V are the horizontal and vertical momentum (eddy) viscosity and K_H and K_V the horizontal and vertical (eddy) diffusivity of heat, respectively. The representation of mixing is very simple and in state-of-the-art ocean models, more advanced formulations [11] are used. In addition,

$$\frac{D}{dt} = \frac{\partial}{\partial t} + \frac{u}{r_0 \cos\theta}\frac{\partial}{\partial \phi} + \frac{v}{r_0}\frac{\partial}{\partial \theta} + w\frac{\partial}{\partial z},$$

$$\nabla_H \cdot (K_H \nabla_H) = \frac{1}{r_0^2 \cos\theta}\left[\frac{\partial}{\partial \phi}\left(\frac{K_H}{\cos\theta}\frac{\partial}{\partial \phi}\right) + \frac{\partial}{\partial \theta}\left(K_H \cos\theta \frac{\partial}{\partial \theta}\right)\right],$$

$$L_u(u,v) = \nabla_H^2 u + \frac{u}{r_0^2\cos^2\theta} - \frac{2\sin\theta}{r_0^2\cos^2\theta}\frac{\partial v}{\partial \phi},$$

$$L_v(u,v) = \nabla_H^2 v + \frac{v}{r_0^2\cos^2\theta} + \frac{2\sin\theta}{r_0^2\cos^2\theta}\frac{\partial u}{\partial \phi}.$$

Slip conditions are assumed at the bottom boundary, while at all lateral boundaries no-slip conditions are applied. At all lateral boundaries and the bottom boundary, the heat flux is zero. As the forcing is represented by a body force over the first layer, slip and no-flux conditions apply at the ocean surface. Hence, the boundary conditions are

$$z = -D, 0: \quad \frac{\partial u}{\partial z} = \frac{\partial v}{\partial z} = w = \frac{\partial T}{\partial z} = 0, \tag{9a}$$

$$\phi = \phi_w, \phi_e: \quad u = v = w = \frac{\partial T}{\partial \phi} = 0, \tag{9b}$$

$$\theta = \theta_s, \theta_n: \quad u = v = w = \frac{\partial T}{\partial \theta} = 0. \tag{9c}$$

The parameters for the standard case are the same as in typical large-scale low-resolution ocean general circulation models and these values are listed in Table 1.

Table 1
Standard values of parameters used in the numerical calculations

$2\Omega = 1.4 \times 10^{-4}$ [s^{-1}]	$K_H = 1.8 \times 10^3$ [m^2 s^{-1}]	$H_m = 250$ [m]
$D = 4.0 \times 10^3$ [m]	$C_p = 4.2 \times 10^3$ [J(kg K)$^{-1}$]	$A_V = 1.0 \times 10^{-3}$ [m^2 s^{-1}]
$\alpha_T = 1.0 \times 10^{-4}$ [K^{-1}]	$r_0 = 6.4 \times 10^6$ [m]	$K_V = 2.3 \times 10^{-4}$ [m^2 s^{-1}]
$\rho_0 = 1.0 \times 10^3$ [kg m^{-3}]	$\tau_T = 7.5 \times 10^1$ [days]	$\Delta T = 20.0$ [K]

Note that the value of A_H will be specified in each of the results below.

Since convection, which occurs in case of an unstable stratification, is not by the hydrostatic model, a representation is needed to obtain stably stratified solutions. In the results below, we use the global convective adjustment procedure as described in Dijkstra et al. [7].

3. The occurrence of wiggles

We focus on the steady state solutions and hence time derivatives are put to zero in Eq. (8e). The equations are discretized in space using a second-order accurate control volume discretization method either on a staggered Arakawa C-grid (see Fig. 5), we refer to this model below as THCM-C, or an Arakawa B-grid (see Fig. 6), we refer to this model below as THCM-B. For the advective transport in the temperature equation, the conservative form is used. After discretization, a system of nonlinear algebraic equations results which can be written as

$$\mathbf{F}(\mathbf{x}, \mathbf{p}) = 0. \tag{10}$$

Here $\mathbf{x}$ is the d-dimensional state vector, consisting of the unknowns (u, v, w, p, T) at the grid points, $\mathbf{p}$ is the p-dimensional vector of parameters and $\mathbf{F}$ is a nonlinear mapping from $R^d \times R^p \rightarrow R^d$. The latter operator is different for B-grid and C-grid versions.

To compute a branch of stationary solutions in a control parameter, say λ, a pseudo-arclength method is used [14]. The branches of stationary solutions $(\mathbf{u}(s), \lambda(s))$ are parameterized by an arclength parameter s. Since this introduces an extra unknown, an additional equation is needed and the tangent is normalized along the branch, i.e.

$$\dot{\mathbf{u}}_0^T(\mathbf{u} - \mathbf{u}_0) + \dot{\lambda}_0^T(\lambda - \lambda_0) - \Delta s = 0, \tag{11}$$

where Δs is the step length, the superscript 'T' denotes the transpose, a dot indicates differentiation to s and $\mathbf{u}_0$ indicates a previous solution computed for $\lambda = \lambda_0$.

The system (10) and (11) is solved by the Newton–Raphson method, combined with the adaptive Shamanskii method, to determine points on the branch of stationary solutions [23]. This method finds isolated steady solutions, regardless of their stability. The linear systems are solved with the GMRES method (an iterative linear systems solver) using MRILU (a multigrid oriented) preconditioning technique [4].

For both THCM-B and THCM-C, the standard horizontal resolution is 4° in the zonal direction, 4° in the meridional direction and 16 equidistant levels in the vertical. To monitor the flow solutions, we will use the maximum of the meridional overturning streamfunction ψ. The quantity ψ measures the zonally averaged volume transport and it is defined as

$$\cos\theta \int_{\phi_w}^{\phi_e} v \, d\phi = \frac{\partial \psi}{\partial z}; \quad \cos\theta \int_{\phi_w}^{\phi_e} w \, d\phi = -\frac{\partial \psi}{\partial \theta}. \tag{12}$$

   The pseudo-arclength continuation starts at the trivial steady solution for $\Delta T = 0$. The latter is used as a control parameter and increased up to $\Delta T = 20$ to find a solution without convective adjustment. Next, the global adjustment procedure is applied to give the stably stratified flow. For the standard value of parameters and $A_H = 1.6 \times 10^7 \, \text{m}^2 \, \text{s}^{-1}$, the stably stratified solution ψ in THCM-C (Fig. 2(a)) is smooth and has about 24 Sv meridional transport. In Fig. 2(b), the horizontal velocities at the surface are plotted (arrows) together with the vertical velocity just below the surface (contour lines). For this relatively large value of A_H, the western boundary current is very diffusive and also the upwelling and downwelling regions are broad. Sinking occurs in the northeast and there is a return flow at depth of opposite direction than the surface flow.

   When A_H is next considered as a control parameter in the pseudo-arclength continuation method and the solution in Fig. 2 is followed to smaller values of A_H, problems start to occur at $A_H = 9.5 \times 10^6 \, \text{m}^2 \, \text{s}^{-1}$. It is not possible to continue below this value and the solution starts to display wiggles, first near the eastern boundary. When for $A_H = 8.0 \times 10^6 \, \text{m}^2 \, \text{s}^{-1}$, ΔT is increased from zero, the Newton–Raphson process has difficulty to convergence beyond $\Delta T = 18.6$ K so the standard value ($\Delta T = 20$ K) cannot be reached. For $A_H = 1.6 \times 10^5 \, \text{m}^2 \, \text{s}^{-1}$, wiggles are already seen at very small values of ΔT. The meridional overturning streamfunction and surface velocities of the solution for $\Delta T = 2.5$ K are plotted in Fig. 3. The solution from
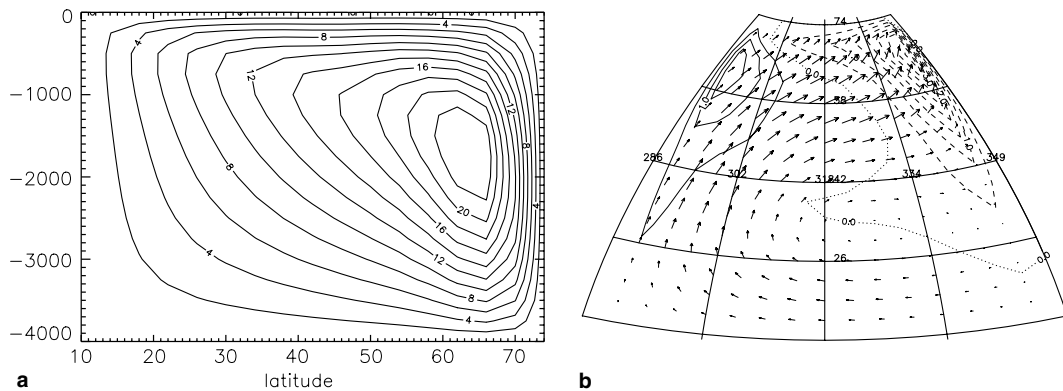

Fig. 2. Equilibrium solutions (with convective adjustment) computed with the THCM-C model. (a) Equilibrium meridional overturning streamfunction (in Sv) and (b) surface velocities for $A_H = 1.6 \times 10^7 \, \text{m}^2 \, \text{s}^{-1}$.
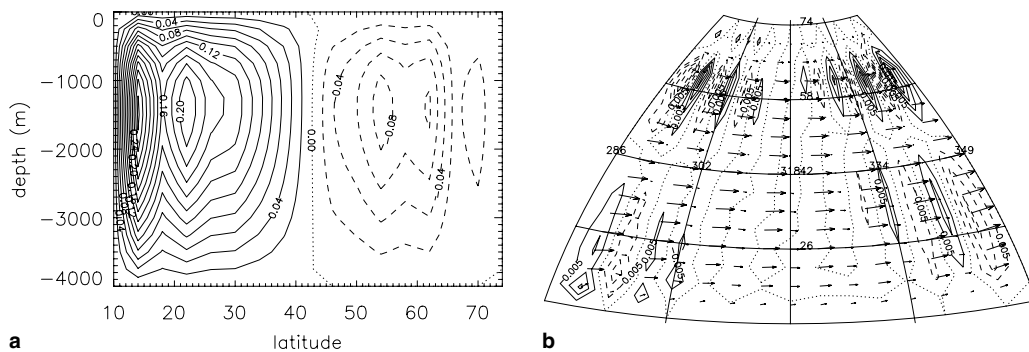

Fig. 3. (a) Equilibrium meridional overturning streamfunction (in Sv) for $A_H = 1.6 \times 10^5 \, \text{m}^2 \, \text{s}^{-1}$ and $\Delta T = 2.5$ K. (b) Surface velocities for the same solution as in (a).
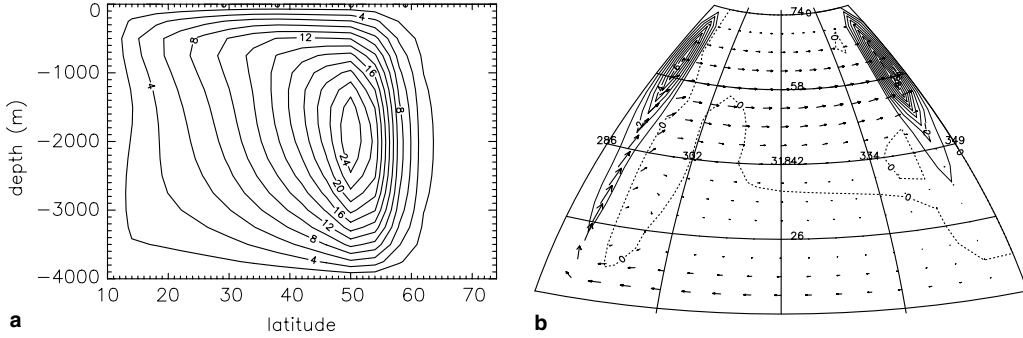
Fig. 4. Steady solution for standard values of parameters (with convective adjustment) as obtained by the THCM-B model through pseudo-arclength continuation. (a) Equilibrium meridional overturning streamfunction (in Sv). (b) Surface velocities.

THCM-C displays wiggles throughout the domain in both ψ (Fig. 3(a)) and the surface velocities (Fig. 3(b)).

The wiggles are not related to the frictional western boundary (Munk) layer [5] as they are still present when the meridional variation of the Coriolis parameter is set to zero. In Dijkstra et al. [7], it was suggested that these wiggles originate at the eastern boundary and that they are due to errors to resolve boundary layers. The thickness of the Ekman layers near the continental walls have a typical width of $\delta_E = (A_H/f)^{1/2}$, where $f = 2\Omega \sin \theta$. Resolving these layers requires a value of A_H larger than

$$A_H \approx \max_{10 \leqslant \theta \leqslant 74} 2\Omega r_0^2 (\Delta\phi)^2 \cos^2\theta \sin\theta, \tag{13}$$

where $\Delta\phi$ is the zonal grid resolution.

However, as this boundary layer is not resolved in the B-grid formulation either for $A_H = 1.6 \times 10^5 \, \text{m}^2 \, \text{s}^{-1}$, one would also expect wiggles to appear in this case. The meridional overturning ψ computed with THCM-B for standard values of parameters is plotted in Fig. 4(a). The overturning flow is confined to the southern latitudes with a maximum volume transport of about 25.9 Sv. The surface velocities (arrows indicate horizontal velocities and contours are of the vertical velocity) of the same solution are plotted in Fig. 4(b) and show a strong zonal flow with a maximum near 50°N. Note that the western boundary current is much stronger and has a smaller zonal scale than the solution in Fig. 2 due to the smaller value of A_H. The upwelling/downwelling regions are also much smaller. The THCM-B solution appears to be smooth and does not suffer from the wiggles appearing on the C-grid.

4. The origin of the wiggles

The results of the previous subsection suggest that high-frequency components of the error, due to lack of resolution in the boundary layers at the eastern wall, are amplified strongly in THCM-C, while hardly so in THCM-B. As they occur at every latitude and also for a zero planetary vorticity gradient, we can simplify the analysis on a f-plane model in Cartesian coordinates. As the wiggles appear already at small thermal forcing (small ΔT), advection of heat is not likely to play a role and we just prescribe a fixed temperature distribution and consider the solutions of the linear momentum and continuity equations. These equations can be written as

$$-fv + \frac{1}{\rho_0}\frac{\partial p}{\partial x} = A_V \frac{\partial^2 u}{\partial z^2} + A_H \nabla_H^2 u, \tag{14a}$$

$$fu + \frac{1}{\rho_0}\frac{\partial p}{\partial y} = A_V \frac{\partial^2 v}{\partial z^2} + A_H \nabla_H^2 v, \tag{14b}$$

$$\frac{\partial p}{\partial z} = \rho_0 T g \alpha_T, \tag{14c}$$

$$0 = \frac{\partial u}{\partial x} + \frac{\partial v}{\partial y} + \frac{\partial w}{\partial z}. \tag{14d}$$

The domain is approximately 5000 km in the x-direction and 7000 km in the y-direction. For convenience we take the domain as square with side lengths $L = 6000$ km and a typical value for f will be 10^{-4} s^{-1}. We redefine the temperature $\rho_0 T g \alpha_T \to T$ and prescribe it over the whole domain as $T = cy + b$.

The nice property of Eqs. (14) is that they allow a relatively simple mode (barotropic/baroclinic) splitting. Integration over the total depth of (14a), (14b) and (14c) using the boundary conditions (9a) shows that, since wind forcing is absent, the vertically averaged horizontal velocities are zero and the vertically averaged pressure $\bar{p}$ is constant. Hence the pressure can be explicitly determined from the temperature field, which gives for the deviation $\tilde{p}$ of the vertically averaged pressure the result

$$\tilde{p} = \int_{-D}^{z} T \, dz' - \frac{1}{D}\int_{-D}^{0}\left(\int_{-D}^{z} T \, dz'\right)dz. \tag{15}$$

Substitution of (15) into (14a) and (14b) gives two equations for the horizontal velocities, which we denote by $\tilde{u}$ and $\tilde{v}$, because they are the deviations from the vertical averaged zonal and meridional velocities, respectively. Once these velocities are known, the vertical velocity is solved from (14d).

When this decomposition is implicitly carried out in the linear system of discretized equations, it will turn out to be possible to compute the amplification factors of the high-frequency components in the solutions.

4.1. C-grid: Discrete equations and barotropic–baroclinic separation

On the C-grid the positioning of the variables is as depicted in Fig. 5. It shows the projections of the 3D cell on which the mass conservation law (continuity equation) is discretized. Central differences are used for the discretization. Since we do not have the v-velocities available at the u-points, the four v-velocities surrounding a u-point are averaged in the discretization of the Coriolis acceleration. The boundary at the east and west coast runs through the u-points. In order to impose the Dirichlet boundary condition for the v-point an average perpendicular to the boundary is taken.

For the rectangular domain, one can represent the matrix form of the discretization in an elegant way using Kronecker tensor products. The Kronecker product is a binary matrix operator that maps two arbitrarily dimensioned matrices into a larger matrix with a special block structure. Given an $n \times m$ matrix A and a $p \times q$ matrix B, then $A \otimes B$ is the $np \times mq$ matrix
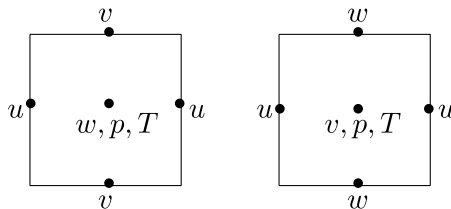

Fig. 5. Positioning of variables in C-grid, topview (left) and vertical cross section (right). The vertical layout is called the Lorenz grid.

$$A \otimes B = \begin{pmatrix} a_{1,1}B & \cdots & a_{1,m}B \\ \vdots & \vdots & \vdots \\ a_{n,1}B & \cdots & a_{n,m}B \end{pmatrix}. \tag{16}$$

The discretized operator associated with mixing of zonal momentum is represented as

$$L_u = A_{\mathrm{H}}(I_z^{uu} \otimes (I_y^{uu} \otimes G_x^{uu} + G_y^{uu} \otimes I_x^{uu})) + A_{\mathrm{V}}(G_z^{uu} \otimes I_y^{uu} \otimes I_x^{uu}), \tag{17}$$

with a similar definition for L_v. Here, I_*^{uu} is an identity matrix and G_*^{uu} is a tridiagonal matrix resulting from the discretization of the second-order derivative. The subscript denotes the considered space direction. In general, the first component in the superscript denotes the destination variable and the second the origination variable. The number of rows/columns of a matrix is the number of unknowns of the destination/origination variable in the direction specified by the subscript. Note that the order of I_x^{vv} is one more than that of I_x^{uu} and the other way around for the y-direction. By writing the equations in matrix form, we implicitly have pinned down the ordering of the unknowns; the horizontal planes are ordered one after another and within a horizontal plane, the unknowns are ordered on lines in x-direction.

The matrices describing the discrete gradient operator are given by

$$B_u = I_z^{uu} \otimes I_y^{uu} \otimes D_x^{up}, \tag{18a}$$

$$B_v = I_z^{vv} \otimes D_y^{vp} \otimes I_x^{vv}, \tag{18b}$$

$$B_w = D_z^{wp} \otimes I_y^{ww} \otimes I_x^{ww}, \tag{18c}$$

where D is a bidiagonal matrix resulting from the discretization of the first order derivative. Note that $I_z^{uu} = I_z^{vv}, I_y^{uu} = I_y^{ww}$ and $I_x^{uu} = I_x^{ww}$. Finally, the discrete Coriolis term can be written as

$$F_u = f\left(I_z^{uu} \otimes M_y^{uv} \otimes M_x^{uv}\right), \tag{19}$$

where M_*^{uv} denotes an averaging in the direction given in the subscript. Using these building blocks, the discrete momentum equations and continuity equations give rise to the linear system

$$\begin{bmatrix} L_u & F_u & 0 & B_u \\ -F_u^{\mathrm{T}} & L_v & 0 & B_v \\ 0 & 0 & 0 & B_w \\ B_u^{\mathrm{T}} & B_v^{\mathrm{T}} & B_w^{\mathrm{T}} & 0 \end{bmatrix} \begin{bmatrix} u \\ v \\ w \\ p \end{bmatrix} = \begin{bmatrix} 0 \\ 0 \\ T \\ 0 \end{bmatrix}, \tag{20}$$

where the right-hand side contains the buoyancy forcing.

In Appendix A, the technical details are provided how the splitting in a barotropic and a baroclinic part is accomplished in the discrete equations. From the resulting system of equations as shown in (35), observe that the barotropic and baroclinic parts can be solved completely independent of each other. Since the right-hand side for the vertical averaged unknowns is zero, it follows that also in the discrete case $\bar{u}$ and $\bar{v}$ are zero and $\bar{p}$ is constant. This is due to the fact that we only have temperature forcing.

The right-hand side of the baroclinic part can be made more explicit. First, we have to determine $\tilde{p}$. To simplify this computation we do it on the continuous counterpart, which will give the same solution since the employed discretization is second-order accurate and hence exact for the linear solutions which follow. So from (15) we find $\tilde{p} = (cy + b)(z + D/2)$. Now the right-hand side can be found. Since there is no dependency on x in $\tilde{p}$, it follows that $B_u \tilde{p} = 0$ in (34). There is however a dependency on y leading to $B_v \tilde{p} = c(z + D/2)$. So the nonzero part of the right-hand side does not vary in horizontal directions. Since, the operations following (34) only act in vertical directions these conclusions carry over to (35). So our problem boils down to

$$\begin{bmatrix} \tilde{L}_u & \tilde{F}_u \\ -\tilde{F}_u^{\mathrm{T}} & \tilde{L}_v \end{bmatrix} \begin{bmatrix} \check{u} \\ \check{v} \end{bmatrix} = \begin{bmatrix} 0 \\ \gamma \end{bmatrix}, \tag{21}$$

where γ is constant for every horizontal plane, say γ_i for the ith plane. For the definition of the other matrices we refer to Appendix A.

In the sequel we will solve this baroclinic part by Fourier transformation, which will allow us to study the influence of high-frequency components on the solution. For completeness, once u, v and p are determined, w can be solved from the continuity equation. The associated system is overdetermined but it is easy to show that the right-hand side is in the range of the matrix.

4.2. C-grid: Fourier analysis

In this section, we solve the baroclinic part (21) using the Fourier sine transformation. By comparing the magnitude of high and low-frequency Fourier components we can predict when wiggles become visible in the solution.

First we discuss the precise form of the Fourier basis functions. Since we have for the u and v variables Dirichlet boundary conditions, we can simply make an odd periodic extension, or equivalently we have to deal with a sine expansion. Say now that we have in x direction N equally-spaced internal points. The Fourier basis vectors for the u-points are $\sin(kj\pi/(N+1))$ where $1 \leqslant j \leqslant N$ for $k = 1, \ldots, N$. The v-points have one more internal point in x-direction. Its Fourier basis vectors are $\sin(k(j - \frac{1}{2})\pi/(N+1))$ where $1 \leqslant j \leqslant N+1$, for $k = 1, \ldots, N+1$. (Note that for $k = N+1$ we obtain a sawtooth basis vector and for k close to $N+1$ it resembles such a vector.) For later reference we also give the length of the deduced eigenvectors: The vector at the u-points has length $\sqrt{(N+1)/2}$ and the one at the v-points has the same length for $k \leqslant N$ but for $k = N+1$ it has length $\sqrt{N+1}$.

Having determined the basis functions we can now go on with finding the eigenvalues (or symbols) of the operators occurring in the matrix of (21). Since the basis vectors are appropriate combinations of elementary complex exponential $\exp(i\phi)$ which in itself is an eigenfunction of difference operators, these basis vectors give us immediately the eigenvalues of G_x^{uu} and G_x^{vv} which are simply $\alpha(k) = -4\sin^2(k\pi/(2(N+1)))/h^2$, where $h = L/(N+1)$, be it that the latter matrix has one more eigenvalue, i.e. for $k = N+1$ an eigenvalue $-4/h^2$.

Applying M_x^{uv} to the Fourier basis function at the v-points leads to:

$$\frac{1}{2}\left[\sin\left(k\left(j + \frac{1}{2}\right)\pi/(N+1)\right) + \sin\left(k\left(j - \frac{1}{2}\right)\pi/(N+1)\right)\right] = \cos(k\pi/(2(N+1)))\sin(kj\pi/(N+1)).$$

So it gives us precisely the eigenvector for the u-points and an eigenvalue $\beta(k) = \cos(k\pi/(2(N+1)))$. Note that there is no contribution for $k = N+1$. Conversely applying M_x^{vu} to the eigenvector at the u-points gives the same eigenvalue.

With the foregoing the matrices of the system (21) can be diagonalized by the Fourier sine transformation and now we have to compute the according Fourier transform of the right-hand side. Since we have already found that the right-hand side is constant for every horizontal plane we have to study in essence the inner products of a basis vector with the constant vector in particular for smooth modes, which are strongly present in the continuous solution, and for highly oscillatory modes, which generate the wiggles. For convenience we introduce $\theta = k\pi/(N+1)$; note that it runs between 0 and π. Herewith the inner product of a constant vector with entries one with the basis function for the u-points in x-direction yields:

$$\sum_{j=1}^{N} \sin(j\theta) = \frac{1}{2i} \sum_{j=1}^{N} [\exp(ij\theta) - \exp(-ij\theta)]$$

$$= \frac{1}{2i} \left[\frac{\exp(i\theta) - \exp(i(N+1)\theta)}{1 - \exp(i\theta)} - \frac{\exp(-i\theta) - \exp(-i(N+1)\theta)}{1 - \exp(-i\theta)} \right] = \frac{1}{2}(1 - (-1)^k)\frac{1}{\tan(\theta/2)}.$$

For small θ we have for odd k the approximation $\tan^{-1}(\theta/2) \approx 2/\theta = 2(N+1)/(k\pi)$. For θ close to π we introduce $\hat{\theta} = \pi - \theta = (N+1-k)\pi/(N+1)$ and find $\tan^{-1}(\theta/2) = \tan(\hat{\theta}/2) \approx \hat{\theta}/2 = (N+1-k)\pi/(2(N+1))$. So the ratio of the magnitude of the high-frequency coefficient (occurring for $k = N$) and that of the low-frequency coefficient (occurring for $k = 1$) (the tangent function is monotonous on this interval) behaves as $1/N^2$.

The same process for the other basis vectors yields:

$$\sum_{j=1}^{N+1} \sin\left(\left(j - \frac{1}{2}\right)\theta \right) = \frac{1}{2i} \sum_{j=1}^{N+1} [\exp(-i\theta/2)\exp(ij\theta) - \exp(i\theta/2)\exp(-ij\theta)]$$

$$= \frac{1}{2i} \left[\exp(-i\theta/2)\frac{\exp(i\theta) - \exp(i(N+2)\theta)}{1 - \exp(i\theta)} - \exp(i\theta/2)\frac{\exp(-i\theta) - \exp(-i(N+2)\theta)}{1 - \exp(-i\theta)} \right]$$

$$= \frac{1}{2}(1 - (-1)^k)\frac{1}{\sin(\theta/2)}.$$

For small θ this is very similar to the previous result. So the magnitude of the low-frequency modes are equal in both cases as may be expected. For θ in the vicinity of π it is different. The result is $\sin^{-1}(\theta/2) = \cos^{-1}(\hat{\theta}/2) \approx 1$. Note that in this case the ratio of the magnitude of high-frequency coefficient and that of the low-frequency mode behaves as $1/N$. Hence the magnitude of the high-frequency mode is in this case much larger than in the previous case.

We now have all ingredients to write down the transformed system resulting in a series of 2×2 systems for the Fourier coefficients of $\check{u}$ and $\check{v}$. From this, we can compute the amplitude of every frequency mode in the solution. We saw that we only have a nonzero right-hand side if k and l are odd. For convenience we also assume N odd, in order to avoid twiddling around with an extra factor $\sqrt{2}$ if $k = N + 1$. For plane i the Fourier transform of system (21) assumes the form

$$\begin{bmatrix} A_H\tilde{\alpha}_{kl} & f\tilde{\beta}_{kl} \\ -f\tilde{\beta}_{kl} & A_H\tilde{\alpha}_{kl} \end{bmatrix} \begin{bmatrix} u_{kl} \\ v_{kl} \end{bmatrix} = \begin{bmatrix} 0 \\ \frac{2\gamma_i}{\tan(l\pi/(2(N+1)))\sin(k\pi/(2(N+1)))(N+1)} \end{bmatrix},$$

where $\tilde{\alpha}_{kl} = \alpha(k) + \alpha(l) + \frac{A_V}{A_H}(\Lambda_{zu})_i, \tilde{\beta} = \beta(k)\beta(l)$, and the factor $(N+1)/2$ is the square of the length of the eigenvectors. In fact, the Fourier coefficients u_{kl} and v_{kl} do also depend on i but we omit this index for convenience since it does not play a role in the sequel.

This system with two unknowns gives for the Fourier coefficient v_{kl} the solution:

$$v_{kl} = \frac{A_H\tilde{\alpha}_{kl}}{A_H^2\tilde{\alpha}_{kl}^2 + f^2\tilde{\beta}_{kl}^2} \frac{2\gamma_i}{\tan(l\pi/(2(N+1)))\sin(k\pi/(2(N+1)))(N+1)}.$$

Due to the zero right-hand side in the first row, the solution for u_{kl} is a factor times that for v_{kl}:

$$u_{kl} = -\frac{f\tilde{\beta}_{kl}}{A_H\tilde{\alpha}_{kl}}v_{kl}. \tag{22}$$

These two expressions give us the amplitude of every frequency mode in the solution, which allows to study its importance. First we consider the importance of the v-field with respect to the u-field, which is determined by

the factor in (22). Since the solution is mainly built up by the low-frequency components, we compute this factor for $k = l = 1$. Now $\tilde{\alpha}_{11} \approx 2\alpha(1) \approx -2\pi^2/L^2$, since $\frac{A_V}{A_H}(\Lambda_{zu})_i$ is in practice chosen as small as possible and is therefore much less than $\alpha(1)$, it follows that

$$\frac{u_{11}}{v_{11}} = \frac{-f\tilde{\beta}_{11}}{A_H\tilde{\alpha}_{11}} \approx \frac{fL^2}{2A_H\pi^2}. \tag{23}$$

For $A_H = 1.6 \times 10^5$ and $A_H = 1.6 \times 10^7$, these values give a ratio of magnitude approximately 1100 and 11, respectively. So for the small value of A_H the horizontal velocity dominates strongly over the meridional velocity and it does less for the large value of A_H. This is reflected in the plots in Section 3.

The foregoing shows that the horizontal velocities dominate in the solution. Therefore, we compute the ratio of the Fourier coefficient for a high-frequency component and that for a low-frequency component of the horizontal velocity in order to determine for which mesh size the considered high-frequency component will become important in the solution. For the latter we simply take $k = 1$, $l = 1$ and for the former we take $k = N$, $l = 1$. A scan along the high-frequency modes $k = N$, l free and the other way around revealed that the chosen high-frequency mode has the largest amplitude. This is already clear if the product of the tangent and the sine is considered which is minimal in the case taken above. So we picked the most critical high-frequency component, which has a sawtooth like behavior in x-direction.

Also A_H is chosen as small as possible and hence $A_H^2\tilde{\alpha}_{11}^2 + f^2\tilde{\beta}_{11}^2 \approx f^2$. The tangent and sine function in the dominator are assumed equal and approximated by $\pi/2(N + 1) = \pi h/(2L)$. Hence the Fourier coefficient is

$$u_{11} \approx -\frac{fL^2}{2A_H\pi^2}\frac{2A_H\pi^2/L^2}{f^2}\left(\frac{2L}{\pi h}\right)^2\frac{2\gamma_i}{N+1} = \frac{1}{f}\left(\frac{2L}{\pi h}\right)^2\frac{2\gamma_i}{N+1}. \tag{24}$$

For $k = N$, $l = 1$, it follows that $\tilde{\alpha}_{N,1} \approx \alpha(N + 1) = 4/h^2$ and $\tilde{\beta}_{N,1} \approx \beta(N) = \sin(\pi/2(N + 1)) \approx \pi h/(2L)$. Herewith the Fourier coefficient becomes

$$u_{N,1} \approx -\frac{f\pi h/(2L)}{(A_H(4/h^2))^2 + f^2(\pi h/(2L))^2}\frac{2L}{\pi h}\frac{2\gamma_i}{N+1} = -\frac{f}{(A_H(4/h^2))^2 + f^2(\pi h/(2L))^2}\frac{2\gamma_i}{N+1}.$$

The ratio of these two expressions is

$$\frac{u_{N,1}}{u_{11}} \approx \frac{f^2(\pi h/(2L))^2}{(A_H(4/h^2))^2 + f^2(\pi h/(2L))^2} = \frac{1}{\left(\frac{8A_HL}{\pi fh^3}\right)^2 + 1} < \min\left(1, \left(\frac{\pi fh^3}{8A_HL}\right)^2\right). \tag{25}$$

This suggests that the mesh size h should be chosen such that

$$h^3 \ll \frac{8A_HL}{\pi f}$$

in order to make high-frequency error invisible with respect to the solution. If the Ekman boundary thickness $\delta_E = \sqrt{A_H/f}$ is defined, and the mesh size is scaled with L, i.e. $\Delta x = h/L$, then this condition becomes

$$(\Delta x)^3 \ll \frac{8}{\pi}\left(\frac{\delta_E}{L}\right)^2 \tag{26}$$

or

$$\Delta x \ll \frac{2}{\pi^{1/3}}\left(\frac{\delta_E}{L}\right)^{2/3}. \tag{27}$$

For $A_H = 1.6 \times 10^5$ we find $\Delta x \ll 0.05$, so $h \ll 300$ km, and for $A_H = 1.6 \times 10^7$ we require $\Delta x \ll 0.22$, so $h \ll 1300$ km. So in our model problem posed at the start of Section 4 the mesh size is about 400 km. Hence $u_{N,1}/u_{11}$ will be close to one for small A_H; this is precisely what is observed in Fig. 3(b).

Remark. It is also interesting to study the ratio for the v_{kl}. This ratio is simply

$$\frac{v_{N,1}}{v_{11}} = \frac{u_{N,1}}{u_{11}} \frac{\tilde{\alpha}_{N,1}}{\tilde{\alpha}_{1,1}\tilde{\beta}_{N,1}} \approx \frac{u_{N,1}}{u_{11}} \frac{\frac{4}{h^2}}{2\left(\frac{\pi}{L}\right)^2 \frac{\pi h}{2L}} = 4\left(\frac{L}{\pi h}\right)^3 \frac{u_{N,1}}{u_{11}}. \tag{28}$$

In the cases studied, the multiplying factor is at most about 500, so there will be large errors in v_{kl}, however since u_{11} is a thousand times larger (derived above), this is not seen in the plot.

This analysis shows that with the smaller value of A_H a strong amplification of the error will occur, while with the larger value of A_H the error will not dominate over the solution. Note that due to the high exponent of h, modest refinement may already result in a large reduction of the unwanted high-frequency components. The conclusion of this elaborate section is that on the C-grid with no-slip boundary conditions the wiggles result from a combination of the averaging of velocities for the Coriolis force, which does not see high-frequency components well, and the centered application of the Dirichlet boundary condition which gives a relative large Fourier coefficient for the high-frequency components resulting from the Fourier transform of the constant.

4.3. B-grid: discretization and Fourier analysis

In short, we will repeat the analysis for the B-grid. The positioning of the variables is depicted in Fig. 6. It shows the projections of the 3D cell on which the mass conservation law is discretized. Also here straightforward central differences are used for the discretization (in the linear constant mesh size case this is equal to finite volume discretization [15]).

Since here u and v coincide, it holds that $L_v = L_u$ and $F_u = f(I_z^{uu} \otimes I_y^{uu} \otimes I_x^{uu})$. Since in the vertical direction the staggering is as on the C-grid we have that D_z^{wp} is equal to that on the C-grid, moreover G_z^{uu} and G_z^{vv} are equal, so we arrive at an equation similar to (35). In the buoyancy driven case the vertical averaged velocities are again zero and the vertical averaged pressure may be any linear combination of a constant and a checkerboard mode. The latter mode is due to the averaging which is necessary for B_u and B_v.

The Fourier basis functions are here only $\sin(kj\pi/(N+1))$. With all ingredients computed in the C-grid case we can immediately pose the system for the Fourier coefficients.

$$\begin{bmatrix} A_H\tilde{\alpha}_{kl} & f \\ -f & A_H\tilde{\alpha}_{kl} \end{bmatrix} \begin{bmatrix} u_{kl} \\ v_{kl} \end{bmatrix} = \begin{bmatrix} 0 \\ \frac{2\gamma_i}{\tan(l\pi/(2(N+1)))\tan(k\pi/(2(N+1)))(N+1)} \end{bmatrix},$$

so the sine is replaced by a tangent and $\tilde{\beta}_{kl}$ is one here. Hence, now v_{kl} is
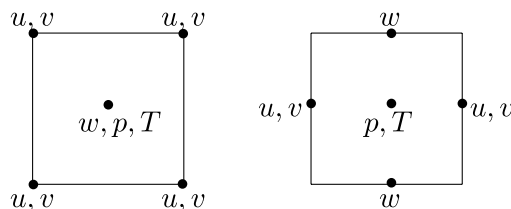

Fig. 6. Positioning of variables in B-grid, topview (left) and vertical cross section (right). The vertical layout is called the Lorenz grid.

$$v_{kl} = \frac{A_H \tilde{\alpha}_{kl}}{A_H^2 \tilde{\alpha}_{kl}^2 + f^2} \frac{2}{\tan(l\pi/(2(N+1))) \tan(k\pi/(2(N+1)))(N+1)} \gamma_i$$

and

$$u_{kl} = -\frac{f}{A_H \tilde{\alpha}_{kl}} v_{kl}.$$

The Fourier coefficient for $k = 1$ and $l = 1$ is equal to the one on the C-grid (24), which has to be the case due to consistency of the discretizations. For $k = N$ and $l = 1$ we find the Fourier coefficient (note that $\tan(1\pi/(2(N+1))) \tan(N\pi/(2(N+1))) = 1$)

$$u_{N,1} \approx \frac{-f}{\left(\frac{4A_H}{h^2}\right)^2 + f^2} \frac{2\gamma_i}{N+1}.$$

Hence the ratio in this case is

$$\frac{u_{N,1}}{u_{11}} \approx \frac{\left(\frac{\pi h}{2L}\right)^2}{1 + \left(\frac{4A_H}{fh^2}\right)^2} < \left(\frac{\pi h}{2L}\right)^2. \tag{29}$$

For the values given the last quantity is approximately 0.01, hence disturbances will not be seen in plots. This approximation is quite sharp for the small value of A_H since then the fraction in the denominator is 0.0016. For the value of $A_H = 1.6 \times 10^7$, it is 16.

It is also interesting to look to the ratio $v_{N,1}/v_{11}$. This is simply $\tilde{\alpha}_{N,1}/\tilde{\alpha}_{11}$ times the ratio for u_{kl} resulting in

$$\frac{1}{2} \frac{1}{1 + \left(\frac{4A_H}{fh^2}\right)^2} < \frac{1}{2} \min\left(1, \left(\frac{fh^2}{4A_H}\right)^2\right). \tag{30}$$

So for the small value of A_H the ratio will be almost a half and hence the mode may be visible in v_{kl}. For the large value of A_H, it is 1/34 and hence it will not be visible. Note that for $k = 1, l = N$ precisely the same result is obtained.

5. Summary and discussion

In this paper, we have tackled a relatively old problem on the origin of wiggles in numerical models of thermally driven midlatitude steady ocean flows. Whereas in B-grid formulations, one can use values of the lateral friction coefficient A_H far below that needed to resolve the lateral Ekman layers, C-grid formulations are restricted to values of A_H for which this boundary layer is resolved. We have shown that this is due to amplification of the high-frequency components in the numerical scheme. This amplification is different in B-grid and C-grid formulations due to the discretization of the Coriolis terms on the different grids.

Our analysis provides more information than, for example, that in Wajsowicz and Gill [22] and Adcroft et al. [1], where one uses dispersion relations to study properties of linearized equations and the numerical scheme chosen. To see this, consider the formal linear equation

$$u_t = Lu - b, \tag{31}$$

where L is a differential operator and b does not depend on t.

In the transient case with $b = 0$ (as in Ref. [1]), the form $\exp(\lambda t - ikx)$ is substituted into (31) and it is found that λ is a function of the wave number k. Note that λ is an eigenvalue of L. In general, λ will be

complex; the real and imaginary part determine the damping and propagation of the wave with wave number k, respectively. If the real part is zero, we find the so-called dispersion relation. In an analogous way one can find such a relation for the discrete equation. Such a relation may reveal that the propagation and damping of some waves on the computational grid is close to zero, i.e. $\lambda \approx 0$, while it is not for the same wave in the continuous case. Or otherwise stated, L times this wave is (nearly) zero. This makes it hard to get rid of these so-called computational modes. Whether we really will see these computational modes in plots is determined by the magnitude of the mode in the initial condition. In the steady case considered here, i.e. $u_t = 0$, we look for a linear combination of terms $\exp(-ikx)$ such that L times this linear combination is precisely b. The coefficients are now determined by b. Such a coefficient may be large if L times the corresponding exponential is nearly zero. So if the eigenvalue λ of L is nearly zero then this may result in a large coefficient for the corresponding exponential.

In summary, the same modes are causing problems in both the transient and stationary cases but to determine the magnitude of such a mode one has to follow different approaches. In the transient case, one has to determine its strength in the initial condition; such an analysis, however, is rarely done [1]. In the steady case, one has to determine the strength of such a mode in b and divide the resulting coefficient by the corresponding eigenvalue. In our case here, such an analysis is crucial in order to determine for which value of the lateral viscosity A_H, the computational mode becomes a critical disturbance of the solution. Our analysis indicates that as soon as the Ekman boundary layer is not resolved, high-frequency components become amplified and hence deteriorate the solution. Since all equations are solved as one system of coupled equations the deterioration extends over the whole domain.

It was pointed out in the previous section that, for the model problem studied, the B-grid is superior to the C-grid. An important question is whether this superiority is still true for smaller mesh sizes. Usually in ocean models, which such a simple representation of mixing, the value of A_H is chosen such that the Munk layer is resolved [5]. This leads to the relation $A_H = 8h^3\beta_0$ where $\beta_0 \approx 2 \times 10^{-11}$ m^{-1} s^{-1}. If we substitute this relation into (25) for the C-grid formulation, it is found that the ratio $u_{N,1}/u_{11}$ becomes independent of the mesh size. So no improvement may be expected from grid refinement. For the ratio $v_{N,1}/v_{11}$ the situation is worse as, according to (28), this ratio will behave as h^{-3}. Fortunately, the ratio of u_{11} and v_{11} given by (23) behaves also in this way if the Munk layer is resolved, and hence $v_{N,1}/u_{11}$ remains bounded. For the B-grid the behavior is much better as the ratio (29) tends to zero if the mesh is refined. Moreover, Eq. (30) shows that $v_{N,1}/v_{11}$ does remain bounded (by 1/2) and consequently $v_{N,1}/u_{11}$ behaves like h^3 and will also tend to zero if the mesh is refined.

For the above mesh-dependent choice of A_H the C-grid solution will not converge to the B-grid solution if the mesh is refined. This numerical phenomenon is due to the used expression for A_H which is only valid for the large mesh sizes generally employed in ocean flow computations. For smaller meshes the expression for A_H must be adapted because it may of course never become smaller than the viscosity of water. In that stage the C-grid solution will converge to the solution of the B-grid upon mesh refinement.

The analysis further suggests some fixes to decrease the amplification of the high-frequency components in the C-grid model. The ''wet point'' method [13] does quite well in reducing the energy of these components but it does not change the fundamental existence of these modes. Although this will be explored in a future study, some preliminary ideas on more efficient fixes are the following. One fix is to put $v = 0$ at points outside of the domain which will affect the order of discretization of the meridional mixing of momentum. It can be shown that amplification is decreased but tests with the single-hemispheric flow revealed that this does not help to compute smooth solutions for substantially smaller values of A_H. Another fix is to take a different averaging for the Coriolis terms near the boundaries, where instead of four points, only two points can be taken. We have not tested this as it may also deteriorate the order of the accuracy of the solution, but it can be shown to lead to lower amplification factors and hence it may be possible to compute flows at lower values of A_H. A third fix is suggested by the work in [16], where the Coriolis terms are discretized using a weighted-averaging scheme.

In conclusion, it is shown here that in these buoyancy driven flows the discretization of the Coriolis terms is crucially important when a boundary layer is not resolved. As the B-grid formulation has this property, it is the desired formulation for this type of flows.

Acknowledgements

Appendix A. Discrete barotropic/baroclinic mode splitting on the C-grid

As a first step we derive an equation for u, v and the vertical averaged pressure. Let e_z^p be the constant unit-length vector of dimension the number of internal p-points in vertical direction, then we introduce the splitting

$$p = e_z^p \otimes \bar{p} + \tilde{p}, \tag{32}$$

where $\bar{p}$ is the vertical averaged pressure field times the square root of the number of pressure points in vertical direction (the square root is only a matter of scaling). Associated with this splitting is the averaging operator $(e_z^p)^{\mathrm{T}} \otimes I_y^{ww} \otimes I_x^{ww}$. Of course, the vertical averaged $\tilde{p}$ is zero, which leads, using the averaging operator, to the condition

$$((e_z^p)^{\mathrm{T}} \otimes I_y^{ww} \otimes I_x^{ww})\tilde{p} = 0. \tag{33}$$

Since, $D_z^{wp} e_z^p = 0$, it follows that $B_w p = B_w \tilde{p}$ and that the averaging operator times B_w is zero. Due to the former, $\tilde{p}$ can be solved independently from the other unknowns from $B_w \tilde{p} = T$ and (33). The latter allows us to determine a system for u, v and $\bar{p}$, by premultiplying the continuity equation by the averaging operator. To facilitate the notation we introduce $\bar{B}_u = (I_y^{uu} \otimes D_x^{up})$, i.e. the horizontal part of B_u, so $B_u = I_z^{uu} \times \bar{B}_u$. Now it holds that $B_u(e_z^p \otimes \bar{p}) = e_z^p \otimes (\bar{B}_u \bar{p}) = (e_z^p \otimes \bar{B}_u)(1 \otimes \bar{p}) = (e_z^p \otimes \bar{B}_u)\bar{p}$. Likewise for $B_v(e_z^p \otimes \bar{p})$. Premultiplying the continuity equation by the averaging operator yields for B_u^{T}:

$$((e_z^p)^{\mathrm{T}} \otimes I_y^{ww} \otimes I_x^{ww})B_u^{\mathrm{T}} = (e_z^p)^{\mathrm{T}} \otimes I_y^{uu} \otimes (D_x^{up})^{\mathrm{T}} = (e_z^p)^{\mathrm{T}} \otimes \bar{B}_u^{\mathrm{T}},$$

similarly for B_v^{T}. The latter results in a 2D horizontal operator acting on the depth-averaged velocities (see Remark below). We have arrived now at the following equation.

$$\begin{bmatrix} L_u & F_u & e_z^p \otimes \bar{B}_u \\ -F_u^{\mathrm{T}} & L_v & e_z^p \otimes \bar{B}_v \\ (e_z^p)^{\mathrm{T}} \otimes \bar{B}_u^{\mathrm{T}} & (e_z^p)^{\mathrm{T}} \otimes \bar{B}_v^{\mathrm{T}} & 0 \end{bmatrix} \begin{bmatrix} u \\ v \\ \bar{p} \end{bmatrix} = \begin{bmatrix} -B_u \tilde{p} \\ -B_v \tilde{p} \\ 0 \end{bmatrix}. \tag{34}$$

Remark. Note that

$$(e_z^p)^{\mathrm{T}} \otimes \bar{B}_u^{\mathrm{T}} = (e_z^p)^{\mathrm{T}} \otimes I_y^{uu} \otimes (D_x^{up})^{\mathrm{T}} = (1 \otimes I_y^{uu} \otimes (D_x^{up})^{\mathrm{T}})((e_z^p)^{\mathrm{T}} \otimes I_y^{uu} \otimes I_x^{uu})$$
$$= (I_y^{uu} \otimes (D_x^{up})^{\mathrm{T}})((e_z^p)^{\mathrm{T}} \otimes I_y^{uu} \otimes I_x^{uu}) = \bar{B}_u^{\mathrm{T}}((e_z^p)^{\mathrm{T}} \otimes I_y^{uu} \otimes I_x^{uu}).$$

So $(e_z^p)^{\mathrm{T}} \otimes \bar{B}_u^{\mathrm{T}} u$ is just the application of $\bar{B}_u^{\mathrm{T}}$ to the (scaled) vertical average of u.

Due to the Neumann conditions at the bottom and surface also the depth-averaged horizontal velocities can be separated from those perpendicular to them. So it holds that also $G_z^{uu} e_z^u = 0$ and $G_z^{vv} e_z^v = 0$ (in fact $e_z^u = e_z^v$). Furthermore, let the orthogonal matrix U_z^{uu} diagonalize the matrix G_z^{uu} and we assume that the first vector in this transformation matrix is the constant vector. We premultiply the first momentum equation by $(U_z^{up})^{\mathrm{T}} \otimes I_y^{uu} \otimes I_x^{uu}$, note that this matrix commutes with B_u, and similarly the second momentum equation. This yields a new system

$$
\begin{bmatrix}
\hat{L}_u & F_u & e_{1z}^p \otimes \bar{B}_u \\
-F_u^{\mathrm{T}} & \hat{L}_v & e_{1z}^p \otimes \bar{B}_v \\
(e_{1z}^p)^{\mathrm{T}} \otimes \bar{B}_u^{\mathrm{T}} & (e_{1z}^p)^{\mathrm{T}} \otimes \bar{B}_v^{\mathrm{T}} & 0
\end{bmatrix}
\begin{bmatrix}
\hat{u} \\
\hat{v} \\
\bar{p}
\end{bmatrix}
=
\begin{bmatrix}
-B_u \hat{\tilde{p}} \\
-B_v \hat{\tilde{p}} \\
0
\end{bmatrix},
$$

where $\hat{L}_u = A_{\mathrm{H}}(I_z^{uu} \otimes (I_y^{uu} \otimes G_x^{uu} + G_y^{uu} \otimes I_x^{uu})) + A_{\mathrm{V}}(\Lambda_{zu} \otimes I_y^{uu} \otimes I_x^{uu}), e_{1z}^p$ is the first unit vector and $\hat{u} = [(U_z^{up})^{\mathrm{T}} \otimes I_y^{uu} \otimes I_x^{uu}] u$, likewise for the other variables with a ˆ. Herewith the system is decoupled in vertical direction. By rearranging we arrive at the desired barotropic–baroclinic separation. In detail, note that the first diagonal element of Λ_{zu} is zero and that the first layer of $\hat{\tilde{p}}$ (recall the horizontal planes of unknowns are numbered one after another) is zero since the vertically averaged $\tilde{p}$ is zero. Hence, the system can be split in two parts:

$$
\begin{bmatrix}
\bar{L}_u & \bar{F}_u & \bar{B}_u & 0 & 0 \\
-\bar{F}_u^{\mathrm{T}} & \bar{L}_v & \bar{B}_v & 0 & 0 \\
\bar{B}_u^{\mathrm{T}} & \bar{B}_v^{\mathrm{T}} & 0 & 0 & 0 \\
0 & 0 & 0 & \tilde{L}_u & \tilde{F}_u \\
0 & 0 & 0 & -\tilde{F}_u^{\mathrm{T}} & \tilde{L}_v
\end{bmatrix}
\begin{bmatrix}
\bar{u} \\
\bar{v} \\
\bar{p} \\
\check{u} \\
\check{v}
\end{bmatrix}
=
\begin{bmatrix}
0 \\
0 \\
0 \\
-\tilde{B}_u \check{\tilde{p}} \\
-\tilde{B}_v \check{\tilde{p}}
\end{bmatrix}.
\tag{35}
$$

Here $\bar{L}_u = A_{\mathrm{H}}(I_y^{uu} \otimes G_x^{uu} + G_y^{uu} \otimes I_x^{uu}), \bar{F}_u = f(M_y^{uv} \otimes M_x^{uv})$ leaving a genuine 2D equation for the vertical averaged variables, i.e. the barotropic part, and $\tilde{L}_u = A_{\mathrm{H}}(\tilde{I}_z^{uu} \otimes I_y^{uu} \otimes G_x^{uu} + G_y^{uu} \otimes I_x^{uu}) + A_{\mathrm{V}}(\tilde{\Lambda}_{zu} \otimes (I_y^{uu} \otimes I_x^{uu})), \tilde{F}_u = f(\tilde{I}_z^{uu} \otimes M_y^{uv} \otimes M_x^{uv}), \tilde{B}_u = \tilde{I}_z^{uu} \otimes I_y^{uu} \otimes D_x^{up}$, where $\tilde{I}_z^{uu}$ and $\tilde{\Lambda}_{zu}$ follow from I_z^{uu} and Λ_{zu} by skipping the first row and column. Moreover $\check{u}$ is just $\hat{u}$ without the variables from the first layer (i.e. $\bar{u}$), similarly for $\check{u}$ and $\check{p}$. The system for these equations is the baroclinic part.

References

[1] A. Adcroft, C.N. Hill, J.C. Marshall, A new treatment of the Coriolis terms in C-grid models at both high and low resolutions, Monthly Weather Rev. 127 (1999) 1928–1936.

[2] A. Arakawa, V.R. Lamb, Computational design of basic dynamical processes of the UCLA general circulation model, Methods Comput. Phys. 17 (1977) 173–265.

[3] A. Arakawa, V.R. Lamb, A potential enstrophy and energy conserving scheme for the shallow water equations, Monthly Weather Rev. 109 (1978) 18–36.

[4] E.F.F. Botta, F.W. Wubs, MRILU: An effective algebraic multi-level ILU-preconditioner for sparse matrices, SIAM J. Matrix Anal. Appl. 20 (1999) 1007–1026.

[5] K. Bryan, S. Manabe, R.C. Pacanowski, A global ocean-atmosphere climate model. Part II. The oceanic circulation, J. Phys. Oceanogr. 5 (1975) 30–46.

[6] H.A. Dijkstra, W. Weijer, Stability of the global ocean circulation: The connection of equilibria in a hierarchy of models, J. Mar. Res. 61 (2003) 725–743.

[7] H.A. Dijkstra, H. Öksüzöglu, F.W. Wubs, E.F.F. Botta, A fully implicit model of the three-dimensional thermohaline ocean circulation, J. Comput. Phys. 173 (2001) 685–715.

[8] H.A. Dijkstra, L.A. Te Raa, W. Weijer, A systematic approach to determine thresholds of the ocean's thermohaline circulation, Tellus 56A (2004) 362–370.

[9] D.B. Enfield, A.M. Mestas-Nuñe, P. Trimble, The Atlantic multidecadal oscillation and its relation to rainfall and river flows in the continental US, Geophys. Res. Lett. 28 (2001) 2077–2080.

[10] M.S. Fox-Rabinovitz, Computational dispersion properties of horizontal staggered grids for atmospheric and ocean models, Monthly Weather Rev. 119 (1991) 1624–1639.

[11] P.R. Gent, J. Willebrand, T.J. McDougall, J.C. McWilliams, Parameterizing eddy-induced tracer transports in ocean circulation models, J. Phys. Oceanogr. 25 (1995) 463–474.

[12] D.B. Haidvogel, A. Beckmann, Numerical Ocean Circulation Modelling, Imperial College Press, London, UK, 1999.

[13] B.M. Jamart, J. Ozer, Numerical boundary layers and spurious residual flows, J. Geophys. Res. 91 (1986) 10,621–10,631.

[14] H.B. Keller, Numerical solution of bifurcation and nonlinear eigenvalue problems, in: P.H. Rabinowitz (Ed.), Applications of Bifurcation Theory, Academic Press, New York, USA, 1977.

[15] Pacanowski, R.C., Griffies, S.M., 2000. MOM 3.0 User Manual. GFDL/NOAA Report.

[16] R. Sadourny, The dynamics of finite-difference models of shallow-water equations, J. Atmos. Sci. 32 (1973) 680–689.

[17] R. Seydel, Practical Bifurcation and Stability Analysis: From Equilibrium to Chaos, Springer-Verlag, New York, USA, 1994.

[18] L.A. Te Raa, H.A. Dijkstra, Instability of the thermohaline ocean circulation on interdecadal time scales, J. Phys. Oceanogr. 32 (2002) 138–160.

[19] L.A. Te Raa, J. Gerrits, H.A. Dijkstra, Identification of the mechanism of interdecadal variability in the north atlantic ocean, J. Phys. Oceanogr. 34 (2004) 2792–2807.

[20] R.C. Wajsowicz, Adjustment of the ocean under buoyancy forces. Part II: The role of planetary waves, J. Phys. Oceanogr. 16 (1986) 2115–2136.

[21] R.C. Wajsowicz, Free planetary waves in finite-difference models, J. Phys. Oceanogr. 16 (1986) 773–789.

[22] R.C. Wajsowicz, A.E. Gill, Adjustment of the ocean under buoyancy forces. Part I: The role of Kelvin waves, J. Phys. Oceanogr. 16 (1986) 2097–2112.

[23] W. Weijer, H.A. Dijkstra, H. Öksüzõglu, F.W. Wubs, A.C. De Niet, A fully-implicit model of the global ocean circulation, J. Comp. Phys. 192 (2003) 452–470.